RSC Advances

ROYAL SOCIETY OF CHEMISTRY

www.rsc.org/advances

Journal Name

RSCPublishing

ARTICLE

Porous (001)-faceted Zn-doped anatase TiO_2 nanowalls and their heterogeneous photocatalytic characterization

Cite this: DOI: 10.1039/x0xx00000x

Received ooth January 2012,
Accepted ooth January 2012

DOI: 10.1039/x0xx00000x

www.rsc.org/

Siti Khatijah Md Saad[a], Akrajas Ali Umar[a*], Hong Quan Nguyen[b], Chang Fu Dee[a], Muhamad Mat Salleh[a] and Munetaka Oyama[c]

The synthesis of poriferous and high-energy (001)-faceted anatase Zn-doped TiO_2 nanowall (ZnTNW) vertically-grown on an ITO substrate is presented. The ZnTNW was prepared using a modified-liquid phase deposition (LPD) method with Zn $(NO_3)_2.xH_2O$ as fluoride scavenger in the presence of hexamethylenetetramine (HMT). In typical procedure, the ZnTNW nanowall with length and thickness of approximately 2 μm and 60 nm, respectively, can be obtained from the reaction during 5 h growth process. XRD analysis shows that the nanowall is anatase structure with dominant high-energy (100) basal plane. Meanwhile, the EDX analysis confirms the presence of Zn in the TiO_2 nanowall. HRTEM analysis result surprisingly reveals that the ZnTNW is single crystalline in nature though it's highly porous (surface and bulk) structure. Photocatalytic properties of the ZnTNW were examined in the degradation of MB. It was found that the ZnTNW exhibit excellent photocatalytic efficiency with kinetic reaction rate, ToN and ToF as high as 0.004 min^{-1}, 760 and 11 min^{-1}, respectively. The photocataltyic performance of ZnTW was found to be higher for about 10 and 50% than the pristine TiO_2 nanowalls (TNW) and (001)-faceted poriferous TiO_2 microtablet (PTM), respectively, reflecting the effective effect of the Zn doping. The ZnTNW may find potentially used in photocatalytic heterogeneous applications.

Introduction

The synthesis of anatase polymorph of TiO_2 characterized with wide-area (001) facet has become the focus of attention recently for enhanced performance in applications that ranges from photocatalysis to optoelectronic devices fabrication and solar cell applications. Its structural, electronic and optical properties have been well-reviewed in recent publications[1, 2]. With the surface containing abundant unsaturated Ti atoms, strained Ti-O-Ti bonds on its outer surface and relaxed-surface energy as high as 1.44 Jm^{-2} makes the (001) faceted-anatase TiO_2 chemically active for wide-range of physico-chemical reactions[3-6]. For example, the water molecules is readily split on the surface of (001) and efficient interfacial charge transfer were observed in the dye-sensitized solar cell utilizing anatase TiO_2 that is rich with this plane. Unfortunately, contrary to its intriguing properties, the synthesis of anatase TiO_2 with (001) plane is challenging and limited due to its nature to easily transform into the (101) face, the most stable and less reactive face, as the result of high-surface energy. Therefore, the chemical synthetic method that enables the preparation of anatase TiO_2 nanostructures that bounded by (001) facets are required and the effort toward this objective should be continuously demonstrated.

So far, several methods are available for the preparation of anatase TiO_2 nanostructure with shape containing large-area (001) facet. Excellent approach was developed by Lu and co-workers. By using TiF_4 as the precursor materials and hydrofluoro acid as the morphology control agent, they successfully realized the formation of large percentage of (001) facet anatase TiO_2 [7-9]. Quite recently, Wang and co-worker demonstrated a new method to synthesis single crystal anatase TiO_2 with dominant (001) facet via a simple hydrothermal decomposition of TiO_2 powder using peroxide. Although high-quality (001) faceted-anatase TiO_2 can be produced using these methods, the structure are atomically smooth surface, rendering low-surface area as well "less-reactivity" as the catalytic and surface reaction favor to occur on the defect or kinks sites[10]. In addition, these methods realize the formation of (001) faceted-anatase TiO_2 in the solution that may limit their usage in particular application, such as solar cell, optoelectronic devices and heterogeneous catalysis. Therefore, the growth of (001) faceted-anatase TiO_2 nanostructure directly on the substrate surface is of considerable important[11].

Although pristine anatase TiO_2 has shown excellent performance in existing applications, metal doping has been discovered to further improve its performance. Transition metals doping, for instance particularly Zn, indicated to enhance its electronic and catalytic properties[12] up to multiple order higher, the result of Fermi level increasing, the reduction of conduction band minimum and the formation of impurity energy level or the increase in the surface oxygen vacancies upon doping[13-15]. These resulted in the shifting of the energy band gap to the visible region, sensitizing its physico-chemical reactivity [16-19]. Our group concentrates on the synthesis of metal and metal oxides nanostructure with controlled shape and morphology [20-26]. Here, we demonstrate the synthesis of Zn-doped anatase TiO_2 nanowall with highly porous (001) faces directly on the substrate surface via a liquid-phase deposition (LPD) method using a new fluoride scavenger, i.e. $ZnNO_3$, instead of boric acid (in normal LPD process)[27-29]. FESEM and HRTEM analysis reveal that the nanowall is constructed by nanocuboid that is assembled resembling a brick-like arrangement. This construction is extended to the surface of nanowall producing highly defect and porous structure on the surface. Such structural properties have made the Zn-doped TiO_2 nanowall exhibited excellent photocatalytic property in the photodegradation of methyl blue with ToN and ToF value as high as 760 and 11 min^{-1}, respectively. This result is much higher compared to undoped TiO_2 nanowall or other TiO_2 morphology, such as PTMs, for multiple orders. The Zn-doped TiO_2 nanowall may find extensive use in solar cell and catalysis.

Experimental section

Materials and methods

Zn-doped TiO_2 nanowall growth on an ITO susbtrate was prepared using a liquid-phase deposition (LPD) method with a modification. In typical procedure, the ZnTNW on the ITO surface were prepared by simply immersed a clean ITO substrate into a 20 mL solution that contains mixture aqueous solution of 5 mL of 0.5 M $(NH_4)_2TiF_6$ (Sigma-Aldrich, USA), and 1 mL of 0.5 M Zn $(NO_3)_2.xH_2O$ in the presence of 1 mL of 0.5 M hexamethylene tetramine (HMT) surfactant. In this study, the Zn $(NO_3)_2.xH_2O$ was used as the fluoride ion scavenger, replacing the boric acid as used in conventional LPD method in growing the TiO_2 films. Prior to the growth process, the solution was ultrasonicated for 2 minutes to obtain a best mixture solution. The growth process was carried out in a temperature controlled-water bath system with growth time of as long as 5 h. The effect of growth temperature was also studied by varying the water bath temperature from 50 to 90 °C. After the growth process, the substrate was removed from the solution, rinsed with a copious amount of pure water and then dried with a flow of nitrogen gas. The entire chemical used in this work were purchased from Sigma-Aldrich Company, USA and used as received. Meanwhile, the ITO was received from Zhuhai Kaivo Optoelectronic Technology Co., Ltd, China with the sheet resistance of approximately 9-22 Ω per square.

The morphology and the crytallinity of the Zn-doped TiO_2 nanowall (ZnTNWs) were examined using Field Emission Scanning Electron Microscope (FESEM) Hitachi S-4800) operating at 2 kV and high resolution transmission electron microscope (HRTEM) Zeiss Libra HRTEM 200 FE operating at 200 kV, respectively. The crystal structure and phase of the samples was characterized by X-ray diffraction technique using BRUKER D8 Advance system with CuKα irradiation (λ=1.541Å) at a scan rate of 10°/min. X-ray photoelectron spectroscopy (XPS) study was performed using XSAM-HS from KRATOS, UK with AlKα radiation. Diffuse reflectance spectroscopy was carried out Perkin-Elmer Lambda 950.

Photocatalytic characterization

The photocatalytic property of the ZnTNWs was evaluated in the degaradation of methylene blue (MB) dye under an illumination of UV light source. An UV-lamp (365 nm) with a power of 5W was used in this study. In typical procedure, 5 mL of 40 ppm of MB was prepared and exposed to the light source. The distance between light source and the MB solution container was fixed at 10 cm. A single slide of ITO (size 1.0 x 1.0 cm^2) containing approximately 0.4 mg of TiO_2 nanocatalyst (measured using gravimetry method) was immersed into the MB solution. The degradation kinetic of MB under the illumination of the UV light source in the absence and the presence of ZnTNWs catalyst were evaluated by analyzing the optical absorbance of MB, particularly at its main absorption band centering at 665 nm, every 10 min of the reaction. The optical absorption was obtained using UV-Vis- NIR Spectrometer (Perkin Elmer, Lambda 900) with spectra resolution 0.2 nm. To verify the role of shape as well as Zn doping on the photocatalytic property, photodegradation of MB in the presence of TiO_2 microtablet and pristine TiO_2 nanowalls were also investigated. In order to obtain the concentration change of the MB solution upon photocatalytic degradation, a calibration curve of absorbance versus MB concentration was also plotted (see Figure S1, Supporting Information).

Results and discussion

Zn-doped TiO_2 nanowall (ZnTNWs) Characterizations

Unlike in the normal liquid-phase deposition method that produces continuous thin film of Ti-complex on the substrate surface, in this work; vertical-oriented and branched-nanowalls of Zn-doped TiO_2 can be realized. Figure 1 shows typical FESEM image of Zn-doped TiO_2 branched-nanowalls (ZnTNWs) grown on ITO substrate prepared using a growth solution containing equimolar (0.5 M) of $(NH_4)_2TiF_6$, Zn $(NO_3)_2.xH_2O$ and (HMT) at a temperature of 90 ^oC for 5 h. As Figure 1 shows, the ZnTNWs is absolutely projected from the substrate surface (see Figure 1C) and grows in high density covering up to approximately 70 % of the substrate surface. The individual nanowall that constructs the ZnTNWs indeed has perfect square-shape morphology (see Figure 1 B) with

width and length can be up to several micrometers and thickness is in the range of 30 to 60 nm. Nevertheless, nanowall with several hundreds of nanometer thick was also obtained. However, its percentage is less than 5% of the product. On the nanowall surface property, interestingly, it is poriferous instead of solid structure. High-resolution FESEM image as shown in Figure 1D-F indicates the surface constructed by fibril structure (diameter and length are ca. 5 and 10 nm, respectively), which is likely projected from the bulk structure of the nanowall. Such property probably makes the nanoplates electronically transparent at such "high' thickness (50 nm) so that the stacked-structure behind the nanoplate can be seen (see Figure 1B). Despite the ZnTNWs is constructed by a perfect-square shape nanowall branches, however, the orientation of the branches are irregular, projecting from a parent nanowall. Nevertheless, the branches projection is mostly formed from the center position of the "parent". High-energy surface atom site at the center of the nanoplate can be the driving force for the re-nucleation and the branches projection. It is true that the projection of nanowall branches from different position on the parent surface was also obtained and their yield is also quite high. However, their formation seemed as the result of collision amongst the adjacent growing branches.

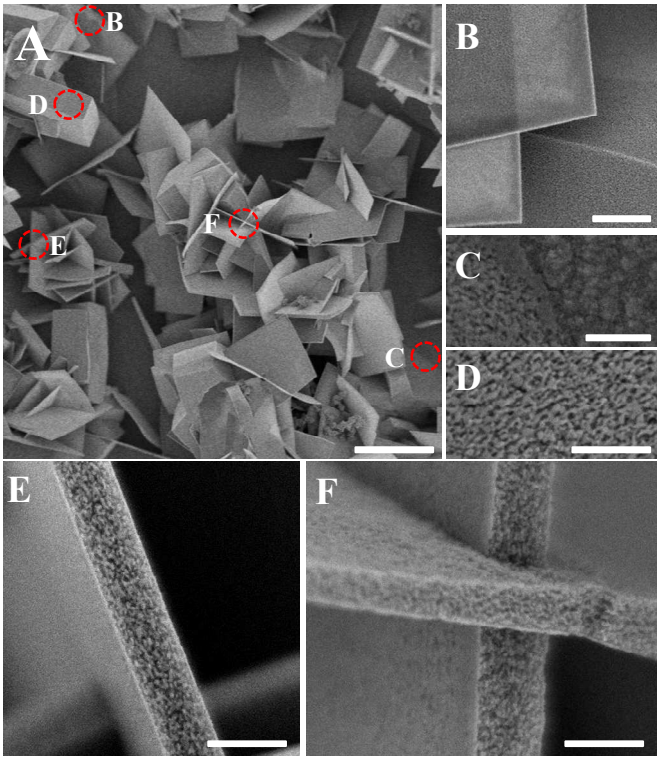

Fig. 1 (A) FESEM image of ZnTNWs growth on the ITO surface prepared using equimolar (0.5 M) of $(NH_4)_2TiF_6$, $Zn(NO_3)_2.xH_2O$ and (HMT). Growth temperature and growth times are 90 ^{o}C and 5 h, respectively. C and D show typical nanowall's base and surface. E and F show typical shape of nanowall. Scale bars are 1 µm for (A), 500 nm for B and 100 nm for C to F.

While the FESEM analysis reveals the surface structure properties of the nanowalls, the high-resolution transmission electron microscopy (HRTEM) analysis reveals its bulk-structure and crystallinity. Figure 2A shows typical nanowall sample observed on the TEM grid. Higher resolution image in Figure 2B and C further confirms the structure constructed by smaller particles, arranged in well-order forming the nanowall geometry. Oriented-attachment process[30] is assumed as the key factor that drives the formation of this structure, a phenomenon that also observed in the formation of poriferous microtablet of TiO_2 on the ITO substrate surface[31]. As observed in the FESEM image, the TEM analysis also indicates that the surface is not a solid (smooth) structure but contains large-scale of voids or pores. Since most surface reaction and charge transfer is more active on defect or high energy sites[32], the TiO_2 with present morphology promises enhanced performance in catalysis and solar cell applications. In contrast to the low-resolution analysis, the high-resolution image reveals that the nanowall is apparently single-crystalline in nature as the appearance of continuous lattice fringe without the presence of twinning or dislocation (see Figure 2D). This infers that the nanowall formation may involve a perfect oriented-attachment process. According to the obtained-lattice fringe spacing value, namely 0.19 nm, it can be understood that the nanoplates is characterized by the (100) plane, which is the second highest energy plane of anatase TiO_2[33].The selected-area electron diffraction (SAED) analysis further confirms the single-crystallinity nature of the structure as well as the formation of (001) face. Figure 2E and 2F are the raw and the reconstructed SAED pattern from the nanowall surface. As can be seen from the raw-pattern, it is true that the "square-shape" SAED pattern, the characteristic of (001) face, cannot be seen directly from the figure due to the absence of some lattice fringes. However, the reconstructed pattern further confirms the formation of square-shape SAED pattern, affirming the (001) face of the nanowall. Judging from the FESEM image in Figure 1 and low-resolution TEM image in Figure 2B-D, the absence of some lattice fringes can be understood simply due to the nature of the surface that contains highly voids structure and porous property at which the electron beam is weakly diffracted or un-diffracted.

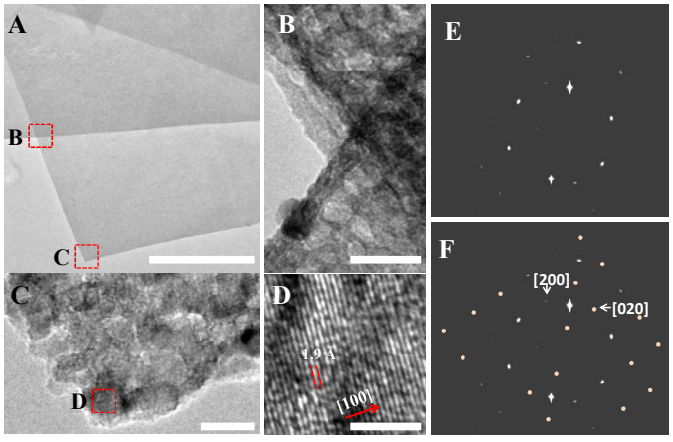

Fig. 2 Low (A-C) and high resolution (D) transmission electron microscopic images of Zn doped TiO2 nanoplate. The low resolution images show the stacking nanoplates and the intersection of the stacked nanoplates (B-C). The high resolution images (D) show a single crystalline nature of nanoplates with

orientation growth of [1 0 0]. E and F are original and reconstructed SAED pattern. Scale bars are 1 µm, 20 nm, 5 nm, 2.5 nm for A, B, C and D, respectively.

As has been mentioned in the Experimental section as the present structure was prepared in a growth solution that is also composed by the Zn+ precursor ($ZnNO_3.H_2O$), the presence of Zn+ in the nanocrystal is expected as an attempt to dope the TiO_2 with this element. However, the HRTEM analysis shows no indication of Zn or ZnO phase presence in the nanocrystals. We then have carried out an X-ray diffraction analysis on the sample to verify the phase and crystallinity of the TiO_2 as well as the Zn presence in the nanocrystal. The result is shown in Figure 3. To our surprise, except the presence of anatase phase of TiO_2 (according to JCPDS No. 21-1272 standard pattern of anatase TiO_2), the X-ray spectrum does not show the presence of either Zn or ZnO phases in the nanocrystal, inferring the occurrence of effective substitution of Zn+ into the anatase TiO_2 nanocrystals. Such process seems valid as the presence of (101) peak position shift to the right from the pristine anatase TiO_2 (see Figure 3b). A detailed curve fitting analysis on the XRD spectra indicates the peaks shifting is as high as 0.01°. Such shifting reveals that there is a reduction in the interplanar distance of the crystal lattice upon Zn atom substitution[34]. This is proven by a higher crystallite size of ZnTNW compared to pristine TNW (See Table S1, Supporting Information). Increasing the crystallite size reflects the reduction of lattice spacing. Unfortunately, although the HRTEM result in Figure 2 suggested that the crystal growth preference is toward [001], the XRD spectra show unclear crystal growth preference. It is true that the (004) peak should be higher or comparable to (101) peak for preferential growth toward this direction. However, this could be due to the nature of TNW surface that is porous exposing stable (101) lattice plane at the body of nanofiber. Thus, the X-ray diffraction from (101) lattice plane still very high. Detailed crystallinity parameter of TNW and ZnTNW is presented in Table S1 (Supporting Information). X-ray energy dispersive analysis (EDX) was further carried out on the sample. The results are shown in inset of Figure 3. As has been expected, the EDX elemental analysis successfully shows the presence of Zn element as well as Ti in the nanowall (see inset B). The elemental mapping of the Zn and Ti in the nanowall indicated a homogeneous dispersion of Zn (shown by green dot) throughout the nanowall, confirming an efficient substitution of Zn into the TiO_2 lattice. As also seen in the inset C and D, the efficient substitution of Zn not only occurs in the nanowall but also in the TiO_2 nanostructures grown on the surface of ITO substrate. One point to be noted here, the O elemental mapping was too strong here due to the contribution of O element of the substrate. Therefore, its distribution in the nanoplate could not be determined.

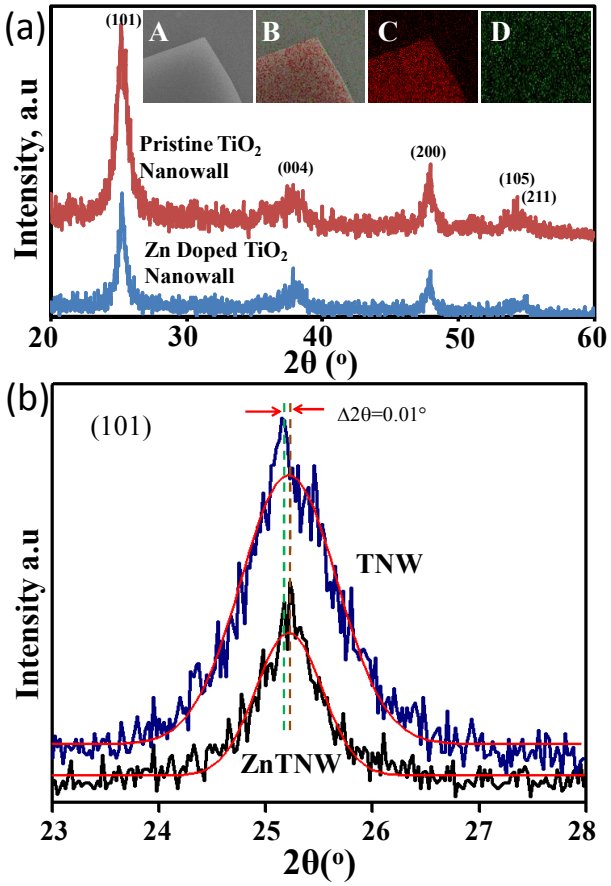

Fig. 3 (a) XRD spectra of pristine TiO_2 nanowall (TNW) and Zn doped TiO_2 nanowall (ZnTNW). Inset show pictographs of unmapped surface of ZnTNW (A) and Ti and Zn mapping (B), Ti (C) and Zn (D) elements mappings. Ti element was indicated by red colour, while the Zn element was green. (b) High-resolution spectra of (101) peaks with curve fitting.

While EDX analysis has confirmed the presence of Zn dope in the nanostructure, which is probably substituted into the TiO_2 crystallite, the X-ray photoelectron spectroscopy (XPS) analysis provides further verification of such process. Figure S2 shows the wide scan XPS analysis without carbon correction indicating the presence of Ti, Zn, and O elements. The fitted spectrum for Ti 2*p* was shown in Figure 4(A) with the presence of two peaks namely Ti2$p_{3/2}$ and Ti2$p_{1/2}$. Both of these peaks can be observed at 458.63 eV and 464.2 eV are however slightly much lower in binding energy compared to other reported research work[35] even though still falls in the Ti2$p_{3/2}$ and Ti2$p_{1/2}$ oxidation state group region. The shifting towards lower binding energy indicates that the investigated TiO_2 nanoplate is indeed are high in oxygen vacancy as might have been contributed by the presence of Zn element in the samples. Regarding the Ti 2$p_{3/2}$ orbital, it is composed of two Gaussian-Lorentzian (GL) mixed function at 459.8 and 458.63 eV, which are corresponding to Ti^{4+} and Ti^{3+} states, respectively. Judging from the intensity of GL function in the 2$p_{3/2}$ orbital, the surface chemistry of the ZnTNW nanowall is characterized by dominant Ti^{3+} state. Similar phenomenon was also observed for the case of pristine TNW. The present result is actually unusual

for TiO_2 nanostructure, which is normally dominated by Ti^{4+} state (for (101) lattice–plane dominated surface. This is an indication of the surface of the nanowall contains highly-reactive five-fold coordinated Ti with strained Ti-O-Ti bond. Novel properties are expected to be generated from this nanostructure. Figure 4 (B) shows the fitted spectrum for oxygen core level O 1*s* of Zn doped TiO_2 nanoplate. From the spectrum, there is the existence of three asymmetric patterns for O 1*s* namely O_L, O_B and O_H. It is well known that the pattern O_L and O_B at 529.25 and 531.3 eV was attributed to the lattice oxygen and bridging oxygen of TiO_2. While the O_H band obtained in the spectrum at 532.1 eV was due to the chemisorbed water on the TiO_2 surface, which leads to the formation of Ti-O-O and Ti-OH. For the OH peak, its intensity is much lower compared to the O_L and O_B. This is an indication of high purity property. The appearance of these asymmetric patterned are normal and in agreement with the reported result. In addition, the peaks appear in the spectrum actually shifted to the lower-energy compared to the pristine TiO_2. This is attributed to the effect Zn doping in the TiO_2 nanocrystals[36].

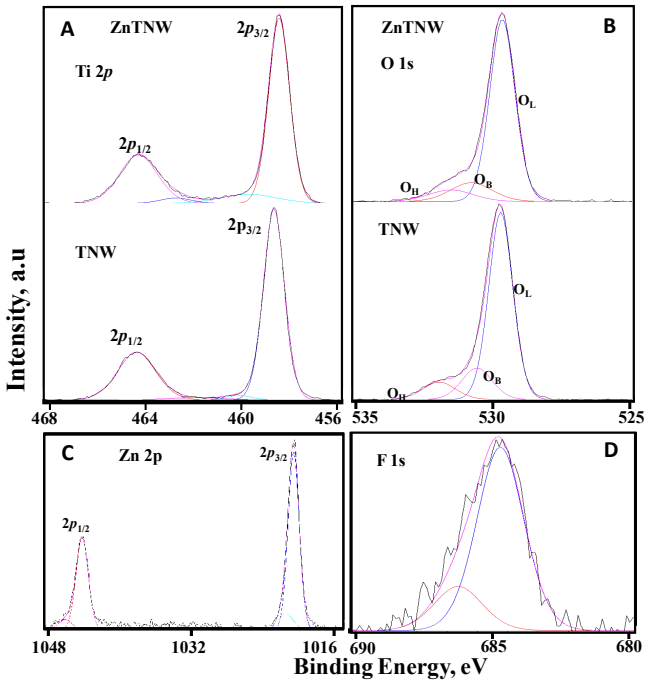

Fig. 4 XPS spectrum of Zn doped TiO_2 nanoparticles and pristine TNW for (A) Ti 2*p*, (B) for O 1*s*, and (C) Zn 2*p* . (D) is spectrum for F 1*s*, proving the surface fluorination.

Along with the Ti, Zn and O spectra, F 1*s* spectrum is also observed in the XPS results (see Figure 4(D)). However, we assumed the presence of fluorine in the nanostructure is not related to lattice impurity but related to the surface adsorption instead[37]. As has been mentioned earlier in the Experimental section, abundant fluorine ions maybe produced during the reaction and they are freely available in the bulk solution because of no fluoride scavenger was used in this study. They may then absorb onto the surface of the nanocrystal and might also have played a particular role in controlling the shape of the nanocrystal. As can be seen from the Figure 4(D), the F 1*s* intensity in Zn-doped TiO_2 is much lower than the pristine TiO_2. This could be as the result of effective scavenging process by the Zn ions.

The exact mechanism of the formation of vertical plate-let structure is not yet clearly understood at this moment. Nevertheless, the crystal plane passivation, (001) plane in this case as confirmed by the XRD analysis, via fluorination and HMT adhesion is assumed as the driving factor for the formation of such morphology[38-41]. It is well-known that the hydrolysis of ammonium hexafluoro titanate by the water may produce fluorine anions in the reaction. They then may easily attach onto and passivate the high energy plane of TiO_2 crystal (001), directing the crystal growth towards [100] direction. XPS analysis result as shown in Figure 4 verifies such fluorination process. Thus, plate-let structure can be formed. However, despite such phenomenon has also been observed in the recently reported result, for example in the formation of TiO_2 nanocube and microtablets, their effect in the formation of plate-let structure in this case is not so crucial but seems as a complement to the significant role of HMT. In our trial, we found that no vertical nanoplate grown on the ITO surface when no HMT in the reaction. To prepare high-density ZnTNWs, the concentration of HMT should be at least 0.4 M. At a lower concentration or in an extreme case in the absence of HMT, TiO_2 films composed of quasi-spherical morphology was produced. The sample shown in Figure 1 was prepared using HMT with concentration of 0.5 M. If the HMT concentration further increases from this value, high-density ZnTNWs with larger thickness and intense branching as well as plate-let overlapping was realized. The results are shown in Figure S3 (Supporting Information). Such un-significant role of surface fluorination effect in the formation of nanowall is indicated by successful growth of Zn-doped TiO_2 nanowall even though limited availability of surface fluorination (indicated by the low-intensity of F 1s peaks in the XPS spectrum) due to the use of Zn ions fluoride scavengers. In addition, to prepare the nanowall, the growth temperature should be around 90 °C, lower temperature, such as 50 and 70 °C; only produces smaller size and low-yield nanowall (see Figure S4 (A) and (C)) (Supporting Information). If the temperature is further lowered, for example at room temperature, neither nanowall nor other nanostructure were formed. Meanwhile, the nanocrystal growth at higher temperature than 90 °C was not obtained due to the boiling of aqueous reaction media.

On the reaction time for nanowall growth, the nanowall were found to formed as earlier 3 h but high-density nanowall growth was obtained at the growth time of 4 h(see Figure S5 (A) and (C)) (Supporting Information) . The density increases with the increasing of the growth time.

The oriented attachment is considered as the main mechanism for the formation of nanowall on the substrate[42]. As judging from the FESEM analysis of the "bulk-volume" structure of the nanowall (see Figure 5), we hypothesized that at the beginning of the reaction nanocuboid structures were formed both in solution and on the surface. Due to containing

high-energy facet, they are attached both onto available nanocuboid on the surface and in the solution to minimize the surface energy. At particular stage at which the reaction chemical potential decreases due to the consumption of precursors nanocuboid shape and size are changed to "nanowires" like structure instead of nanocuboid. Thus, this new structure constructs the surface of the nanowall, forming highly-porous nanowall surface. On the branched-nanowall formation, it is considered due to the re-nucleation of nanocuboid onto the higher-energy site of the nanowall, namely at the centre position of the nanowall. Considering the size of the nanowall branches, its formation is predicted to occur at the earlier stage of the growth process. It is true that the nanowall branches are also observed at non-center position of the main nanowall. However, their formation is due to the collision of adjacent growing nanowalls.

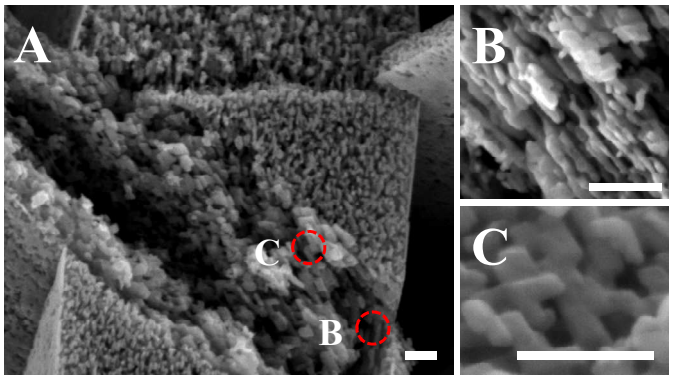

Fig. 5 (A-B) FESEM image of "bulk-volume" structure of the nanowall showing nanocuboid stacking. (C) High-resolution FESEM image showing detailed structure of nanocuboid. Scale bars are 100 nm.

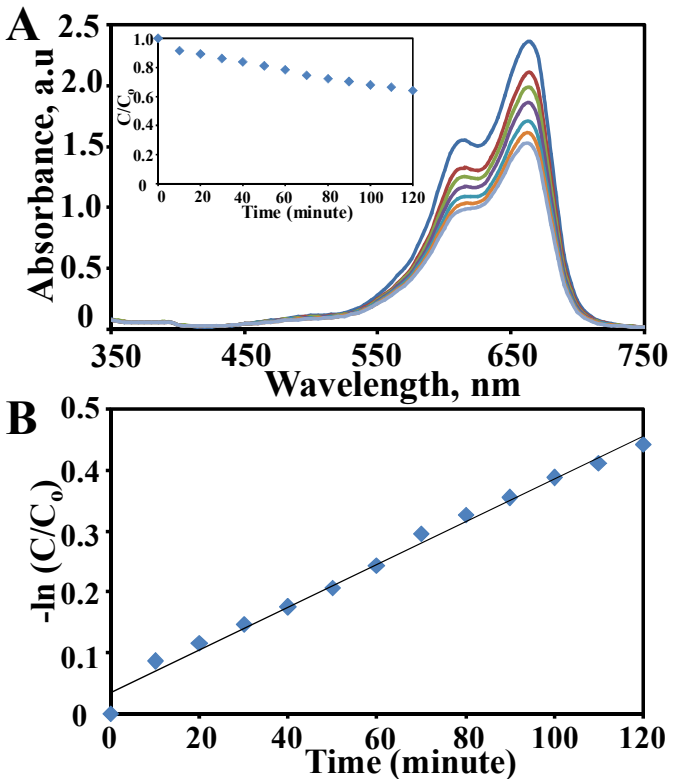

Fig. 6 Typical absorbance (A) and reaction kinetic rate (B) for MB degradation under UV irradiation in the presence of ZTNW nanocatalyst. Inset in A shows the percent degradation of MB during the reaction.

Heterogeneous photocatalytic characterization

A heterogeneous catalytic property of ZnTW was investigated by photodegradation of MB under UV lamp at wavelength of 365 nm. Figure 6A shows typical dynamic absorption spectra of MB during the photocatalytic degradation under UV light exposure. As the Figure 6A reveals, the concentration of MB effectively decreases with the increasing of time during the photocatalytic degradation reaction that is indicated by the decreasing in the absorption intensity at 665 nm. Inset in Figure 6A shows its corresponding degradation kinetic of MB in the presence of ZnTNW obtained by plotting the absorbance value at the peak position over the reaction time.

Table 1. Nanocatalyst properties and photocatalytic parameter.

Sample	S_{BET} ($m^2\ g^{-1}$)	Catalyst Weight (mg)	Reaction Rate, k (min^{-1})	ToN	ToF (min^{-1})
TNW	114.8	0.4	0.0029	689.1	9.84
ZTNW	114.9	0.4	0.0035	759.52	10.85
PTM	160.9	0.7	0.00418	367.97	5.26

As can be seen from the figure, the MB's significantly decreases during the reaction process and reduced to approximately 36% at the reaction course of 120 min. By considering the initial MB concentration of 40 mg L^{-1}, the final concentration is equivalent to 25.8 mg L^{-1}. By taking into account the specific surface area of ZnTNW nanocatalyst obtained from BET analysis of as high as 0.050 m2 and the dynamic cross-section of MB molecules as high as 197.2 $Å^2$, these result is equivalent to turnover number (ToN) and turnover frequency (ToF) as high as 760 and 11 min^{-1},

respectively. Although, the ToN and ToF values of the system is marginal over recently reported results, however, in term of heterogeneous photocatalytic reaction in which molecules adsorption onto the catalyst surface become a crucial issues due to the presence of substrate surface effect as well as solid-liquid interface barrier that may give repulsion force to the approaching molecules, this result is considerably high. In addition, because not all the available surface area is available for MB molecules attachment, for example the lower-level surface, the ToN and ToF should be much higher compared to this values.

By considering the amount of ZnTNW nanocatalyst available on a single slide substrate, approximately 0.4 mg, the present result is 100 times higher compared to the reported result under a homogeneous catalytic reaction. This could be directly related to the following reasons: Firstly, as judged from the XRD and HRTEM results, the presence of large-area of high-energy surface of (001), the available highest surface plane available for anatase TiO_2, that may facilitate effective adsorption and degradation of MB molecules. Analysis of the catalytic activity of ZnTNW in the dark (see curve b in Figure S6, supporting Information), the ZnTNW has readily catalyzed the degradation reaction of MB. It is indicated by significantly high MB degradation (approximately 6%) for the immersion time of 120 min. It has been well known that the (001) plane of anatase TiO_2 is also readily split the water molecules under no external applied field. Secondly, the ZnTNW possesses a high-surface area for surface reaction. BET analysis revealed that the specific surface area of ZnTNW on a single ITO slide is as high as 0.050 m^2 or equivalent to 114.69 g m^{-2} (See Supporting Information for detailed BET analysis). Despite not all the area may involve in the surface reaction, the high-energy property of (001) plane of anatase TiO_2 may facilitate high-efficiency heterogeneous catalytic degradation of MB. To further verify the unique effect of such high-energy plane, the photodegradation rate analysis was carried out. The result is shown in Figure 6B. Based on this result, it is found that the reaction follow a first-order reaction kinetic with a rate as high as 0.0035 min^{-1}, in which the catalytic efficiency solely depend only on the surface reactivity of the nanocatalyst. This reflects that, as the surface of nanocatalyst covered by the MB molecules decreases with time due to MB degradation, the formation of OH- radical ion enhances as the result of facile acceptance of photoexcited electrons by the water molecules[43]. Thus, linearly accelerate the degradation process.

We further examined such effect by varying the catalyst concentration in the reaction by simply introducing up to four ITO slides containing ZnTNW nanocatalyst. The result is shown in Figure 7. As can be seen from the figure, the degradation rate linearly increases when the number of ITO slide containing the ZnTNW nanocatalyst increase in the reaction. For example, the reaction rate is almost double when two slide containing nanocatalyst used in the reaction, namely from 36% to 62%. However, the reaction rate only increases to approximately 70 and 80% when the number of slides increases to three and four, respectively. Although "non-linear" increase in the degradation rate when the amount of catalyst increases in the reaction, we thought that the reaction still obeys first order reaction kinetic. These results could be simply related to the design of the container for the MB solutions that makes the placement of the slides as well as the placement for the UV light source not optimized. Thus, linear increase in the degradation rate as the amount of nanocatalyst increase was not achieved.

The effect of light source irradiation on the degradation of MB can be neglected here because of low-power UV light source was used in this study (5 W). Analysis of the effect of light irradiation on the MB degradation further verified this analysis (see curve a Figure S6, Supporting Information).

So far, the ZnTNW has shown highly efficient catalytic property on the photodegradation of MB. To obtain the extent of Zn doping on the nanostructure, pristine TiO_2 nanowalls (TNW) catalytic properties in the degradation of MB was also examined. The result is shown in Figure 8A (curve a). As the Figure 8A reveals, the TNW exhibits high-efficient catalytic properties in the degradation of MB. It was found that, for a reaction time of 120 min, the concentration of MB changed from 40 mg L^{-1} to 27.35 mg L^{-1}, which is equivalent to a decreasing as high as 31.6%. Kinetic analysis found that the degradation rate is as high as 0.0029 min^{-1} on the TNW system. A decreasing as high as 35.9% or degradation rate of 0.0035 min^{-1} is for the case of ZnTNW for comparison. It is true that this result shows only relatively small improvement of Zn doped-TNW (ZnTNW) compared to the pristine one. The high-efficiency of TNW can be understood as the result of the TNW possesses large-area of (001) high-energy facet, so that efficient catalytic photodegradation can be readily achieved on the pristine TNW. Nevertheless, it is an indication of the improved performance of TNW when doped with the Zn.

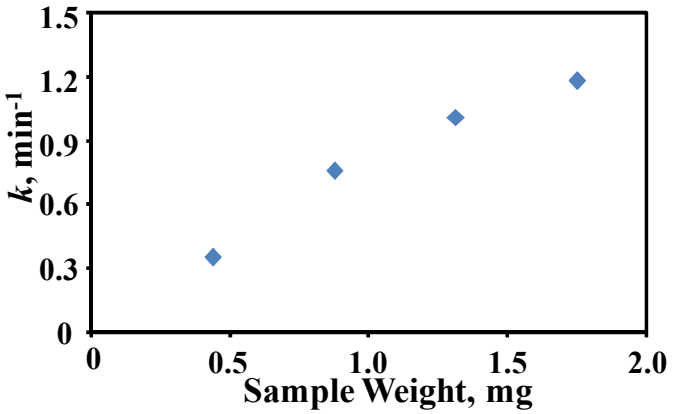

Fig. 7 Kinetic rate of MB degradation (*k*) for different nanocatalyst weight.

In order to further verify the specialty of the presence structure of anatase TiO_2, we compared the catalytic performance with difference structure of TiO_2, namely poriferous TiO_2 microtablet (PTM) (see Figure S7, Supporting Information), which is also characterized by high-energy plane of (001)[31]. The result for kinetic degradation analysis is shown

in Figure 8A (curve c). As can be seen from the figure, it is true that the degradation kinetic rate for PTM is relatively higher than the ZnTNW for about 10%. However, one point to be noted here, since the specific surface area of PTM used here is 0.1227 m^2, which is doubly higher than the ZnTNW, its ToN is inferior over the ZnTNW system. The results are shown in Figure 8B. The detailed properties and catalytic performance of ZnTNW, TNW and PTM is summarized in Table 1. On the basis of these result it can be worth mentioned that the ZnTNW exhibit peculiar catalytic property due to possessing large-scale high-energy facet and Zn doping.

While the present nanostructure has been proven to be superior over other morphologies, the role of Zn doping in the photocatalytic performance was also verified. ZnTNW with three different Zn contents were prepared by introducing zinc salt with concentration of 0.2, 0.5 and 1.0 mM into the standard growth solution. From this reaction, ZnTNW with Zn content as high as 4.77, 7.65 and 2.32 %, respectively, were produced. In typical procedure, it was found that the photocatalytic performance increases with the increasing of the Zn doping concentration. For example, the photodegradation kinetic rate enhanced from 0.0021 min^{-1} to 0.0035 min^{-1} if the concentration of Zn ions content (from the EDX analysis) elevated from 2.32 to 7.65%. The results are shown in Figure S8 (Supporting Information). Although, the improvement is not linearly correlated to the Zn content, this result more or less provides a clear evidence of the role of Zn doping in the improvement of the photocatalytic performance of the ZnTNW. We believed that the performance can be further improved to an optimum performance if Zn content can be further be modified. We attempted to synthesize the ZnTNW with higher concentrations by increasing the zinc salt concentration in the reaction. Unfortunately, further increase in the zinc salt concentration produced ZnTNW nanocrystals with lower Zn content. For example, the Zn content in the sample prepared using 1.0 mM zinc salt is lower than the one prepared using 0.5 mM. It was also found that the structure stability of the ZnTNW decreased with the increasing of zinc salt concentration in the reaction, the result of distortion of growth kinetic condition in the reaction upon the presence of higher concentration of the zinc salt. Nevertheless, the attempt to find the optimum condition is progress.

To further elucidate the effectiveness of the structure and Zn-doping effects on the photocatalytic properties, the extent effect of the light absorption on photocatalytic performance by the ZnTNW was evaluated by diffuse reflectance spectroscopy. The result is shown in Figure S9, Supporting Information). In typical process, it was found that both samples (pristine and Zn-doped TNW) surprisingly exhibit a relatively lower reflectance – independent of the wavelength - compared with the standard Degussa P25 sample[44]. At UV region, for example, which is associated with the excitonic character, the reflectance is as low as 6%. We thought that this could be related to the strong absorption of UV light by the ITO-glass substrate instead of ZnTNW because of transparent and porous nature of the nanowall sample. Meanwhile, at the visible region (400 to 800), lower reflectance can be associated with the porous nature of the TNW surface, which may behave as light cavities at this wavelength region. The enhancement of defect related absorption can also be considered for the increasing of the light absorption in this region. Thus, the effect of light absorption enhancement to the improvement of the photocatalytic activity can be simply neglected. Nevertheless, the ZnTNW exhibits little bit lower reflectance than the pristine TNW. This is a strong evidence for enhanced-electronic excitation in the nanostructure upon doping. It has been well-known that during the photo-irradiation of TiO_2, the electrons are excited to the conduction band (CB) of TiO_2 while leaving the hole at the valence band (VB). The hole in VB then reacts with water molecules producing hydroxyl radicals. Meanwhile, the electron in CB will reduce the formed oxygen in water, forming oxide anions radicals. The oxide anion radical will then react with water that again produces the hydroxyl radical ($OH^{\bullet}$). Finally, the $OH^{\bullet}$ radical will react with MB, resulting in the MB degradation.

During the MB degradation process, the adsorption of O_2 by TiO_2 was necessary to produce the superoxide ($O_2^{\bullet}$) radicals as these radicals will then helps in producing other more reactive radical from hydroxyl groups that exist in the solution. The $OH^{\bullet}$ radical played crucial parts in the degradation of MB due to its lower energy of 2.8 eV. As has been well known that the surface reactivity of the (001) plane was much higher than the typical (101) plane of TiO_2, with surface energy of 1.44 J m^{-2}. Higher surface reactivity contributes to much higher $O_2^{\bullet}$ adsorption on the surface of TiO_2.

The improvement of the photocatalytic properties of the TNW upon Zn doping can be understood from the point of view of: (i) Enhancement of surface activity due to the increasing of surface oxygen vacancy density and impurity energy level[15]. XPS analysis as shown in Figure 4B validates such process as the energy state of O 1s decreases for several orders, which is the key parameter for hydroxyl radical formation, upon doped with Zn. This will further enhance the surface energy for several orders higher, producing more reactive surface to facilitate active $O_2^{\bullet}$ adsorption on the surface. (ii) Increasing of Fermi level energy and the reduction of conduction band minimum when the TNW doped with the Zn[45]. This in turn lower the energy required to photoexcite electron from the valence band. . Diffuse reflectance spectra as shown in Figure S9 confirms such energy gap lowering as increasing of the UV light reflected by the ZnTNW. Improvement of hydroxyl radical formation is expected from this process. Hence, higher photoreactivity are expected to occur on the ZnTNW compared to pristine TNW or PTM

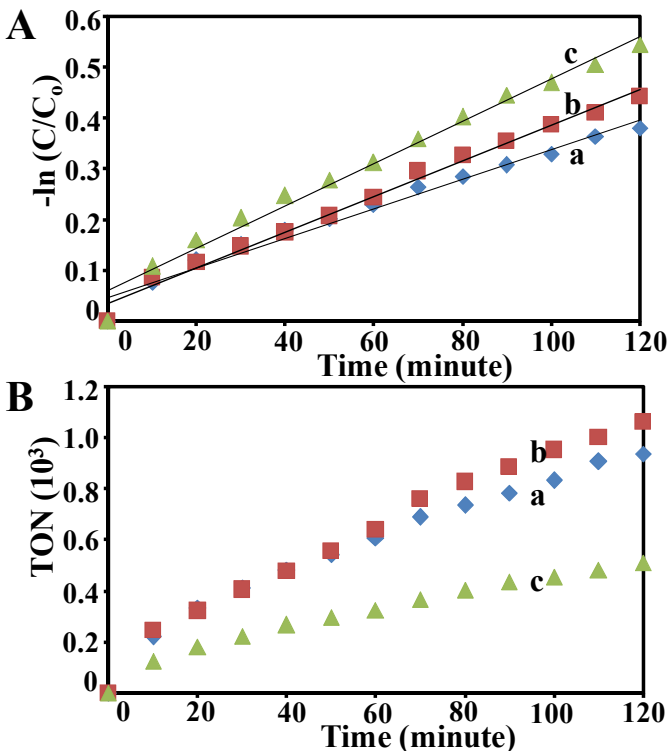

Fig. 8 (A) Kinetic rate of MB degradation under UV irradiation in the presence of different nanocatalyst morphology, TNW (a), ZTNW (b) and PTM (c). (B) is their corresponding ToN analysis results.

Considering the morphology of the ZnTNW composed of fibrous-surface structure with (001) high-energy lattice-plane, the nanostructure may be exposed to a structural deformation as the cost of photocatalytic activity. We carried out FESEM analysis on the after use sample to confirm its chemical stability. The result is shown in Figure S10. Interestingly, despite high-energy plane with fibrous morphology, the sample shows no sign of structural damage or annealing, confirming the nanostructure feature excellent chemical stability property. Thus, it should find a potential use in photocatalysis, sensor or solar cell applications.

The presence photocatalytic performance is evaluated by considering the specific surface area obtained from BET analysis (see Nitrogen adsorption characteristic in Supporting Information) and its surface chemical state is interpreted via XPS. It is true that the active site for catalytic reaction on the surface of catalyst should be examined via temperature programmed desorption (TPD) or temperature programmed reduction (TPR). However, due to the unavailability of the apparatus, the active site is approximated using the BET surface area analysis result. This is assumed to be applicable because the BET is solely based on the analysis of nitrogen gas adsorption and desorption on the TiO_2 nanostructure. Nevertheless, the active site is predicted to be less than the BET surface area since the adsorption of the MB molecules during the photodegradation should be on the most accessible site only, instead on the avalaible surface area. Therefore, the value of the ToN and ToF should much more higher compared to ones presented earlier. Though, the attempt to examine the active catalytic site of the TNW is being pursued and the result will be reported separately.

Conclusions

Zn-doped anatase nanowall with (001) facet and porous structure has been synthesized directly on the ITO substrate surface. The novel structure is constructed by nanocuboid structures that are arranged in a brick-like assembly, producing high-porous property. The (001) high-energy plane nanowall formation is assumed due to the combinative effect of HMT and surface fluorination process during the growth process. Owing to its uniques morphology with high-energy (001) facet and efficient Zn metal doping, the ZnTNW exhibited superior heterogeneous catalytic property over other structure with rich (001) faces, such as poriferous TiO_2 microtablet (PTM), as well aspristine TNW with ToN and ToF in photocatalytic degradation of MB as high as approximately 760 and 11 min^{-1}, respectively. The ZnTNW may find potential used in heterogeneous catalytic, sensors and solar cell applications.

Acknowledgements

The authors would like to acknowledge Universiti Kebangsaan Malaysia and Ministry of Higher Education (MOHE), Malaysia for funding this work under research grants HiCOE Project and FRGS/1/2013/SG02/UKM/02/8. The authors also are grateful for the financial support received from Ministry of Science, Technology and Innovation (MOSTI), Malaysia for the funding under Science Fund grant (06-01-02-SF1157).

Notes and references

a Address here. Institute of Microengineering and Nanoelectronics, Universiti Kebangsaan Malaysia, 43600 UKM Bangi, Selangor, Malaysia. E-mail: akrajas@ukm.edu.my.
b Address here. Dept. Materials Science and Engineering, National Chiao Tung University, Hsin Chu, Taiwan, ROC
c Address here. Department of Material Chemistry, Graduate School of Engineering, Kyoto University, Nishikyo-ku, Kyoto, 615-8520, Japan

† Electronic Supplementary Information (ESI) available: FESEM images of Zn doped TiO_2 prepared under different temperature, HMT and growth time and poriferous microtablet TiO_2 (PTM). See DOI: 10.1039/b000000x/

1. W.-J. Ong, L.-L. Tan, S.-P. Chai, S.-T. Yong and A. R. Mohamed, *Nanoscale*, 2014, **6**, 1946-2008.
2. E. J. W. Crossland, N. Noel, V. Sivaram, T. Leijtens, J. A. Alexander-Webber and H. J. Snaith, *Nature*, 2013, **495**, 215-219.
3. X. Zhao, W. Jin, J. Cai, J. Ye, Z. Li, Y. Ma, J. Xie and L. Qi, *Advanced Functional Materials*, 2011, **21**, 3554-3563.
4. S. M. Roopan, F. N. Khan, J. S. Jin and R. S. Kumar, *Res Chem Intermediat*, 2011, **37**, 919-927.
5. H. G. Yang, C. H. Sun, S. Z. Qiao, J. Zou, G. Liu, S. C. Smith, H. M. Cheng and G. Q. Lu, *Nature*, 2008, **453**, 638-641.
6. J. Yu, J. Fan and K. Lv, *Nanoscale*, 2010, **2**, 2144-2149.
7. G. Liu, C. Y. Jimmy, G. Q. M. Lu and H.-M. Cheng, *Chemical Communications*, 2011, **47**, 6763-6783.
8. W. Yang, J. Li, Y. Wang, F. Zhu, W. Shi, F. Wan and D. Xu, *Chemical Communications*, 2011, **47**, 1809-1811.

9. Y. Luan, L. Jing, Y. Xie, X. Sun, Y. Feng and H. Fu, *ACS catalysis*, 2013, **3**, 1378-1385.
10. Y. Wang, H. Zhang, Y. Han, P. Liu, X. Yao and H. Zhao, *Chemical Communications*, 2011, **47**, 2829-2831.
11. B. Liu and E. S. Aydil, *Chem. Commun.*, 2011, **47**, 9507-9509.
12. S. Wang, H. Qian, Y. Hu, W. Dai, Y. Zhong, J. Chen and X. Hu, *Dalton T*, 2013, **42**, 1122-1128.
13. L. Yang, Y. Zhang, W. Ruan, B. Zhao, W. Xu and J. R. Lombardi, *Journal of Raman Spectroscopy*, 2010, **41**, 721-726.
14. G. Zhu, Z. Cheng, T. Lv, L. Pan, Q. Zhao and Z. Sun, *Nanoscale*, 2010, **2**, 1229-1232.
15. K.-P. Wang and H. Teng, *Phys Chem Chem Phys*, 2009, **11**, 9489-9496.
16. F. Huang, Q. Li, G. J. Thorogood, Y.-B. Cheng and R. A. Caruso, *J Mater Chem*, 2012, **22**, 17128-17132.
17. Z. Ali, S. N. Cha, J. I. Sohn, I. Shakir, C. Yan, J. M. Kim and D. J. Kang, *J Mater Chem*, 2012, **22**, 17625-17629.
18. K. Assaker, C. Carteret, T. Roques-Carmes, J. Ghanbaja, M.-J. Stebe and J.-L. Blin, *New J Chem*, 2014.
19. M. E. Fragala, I. Cacciotti, Y. Aleeva, R. Lo Nigro, A. Bianco, G. Malandrino, C. Spinella, G. Pezzotti and G. Gusmano, *Crystengcomm*, 2010, **12**, 3858-3865.
20. A. Balouch, A. A. Umar, S. T. Tan, S. Nafisah, S. K. Md Saad, M. M. Salleh and M. Oyama, *Rsc Adv*, 2013, **3**, 19789-19792.
21. A. Balouch, A. Ali Umar, A. A. Shah, M. Mat Salleh and M. Oyama, *Acs Appl Mater Inter*, 2013, **5**, 9843-9849.
22. A. Ali Umar and M. Oyama, *Crystal growth & design*, 2006, **6**, 818-821.
23. A. Ali Umar, M. Oyama, M. Mat Salleh and B. Yeop Majlis, *Crystal Growth & Design*, 2010, **10**, 3694-3698.
24. S. T. Tan, A. A. Umar, A. Balouch, M. Yahaya, C. C. Yap, M. M. Salleh and M. Oyama, *Ultrasonics sonochemistry*, 2014, **21**, 754-760.
25. A. A. Umar and M. Oyama, *Crystal Growth and Design*, 2008, **8**, 1808-1811.
26. A. A. Umar and M. Oyama, *Crystal Growth and Design*, 2007, **7**, 2404-2409.
27. S. Deki, H. Y. Y. Ko, T. Fujita, K. Akamatsu, M. Mizuhata and A. Kajinami, *The European Physical Journal D-Atomic, Molecular, Optical and Plasma Physics*, 2001, **16**, 325-328.
28. A. A. Umar, M. Y. A. Rahman, S. K. M. Saad, M. M. Salleh and M. Oyama, *Applied Surface Science*, 2013, **270**, 109-114.
29. W. Shao, F. Gu, L. Gai and C. Li, *Chem Commun*, 2011, **47**, 5046-5048.
30. D. Li, M. H. Nielsen, J. R. I. Lee, C. Frandsen, J. F. Banfield and J. J. De Yoreo, *Science*, 2012, **336**, 1014-1018.
31. A. Ali Umar, S. Nafisah, S. K. Md Saad, S. Tee Tan, A. Balouch, M. Mat Salleh and M. Oyama, *Sol Energ Mat Sol C*, 2014, **122**, 174-182.
32. A. L. Linsebigler, G. Lu and J. T. Yates, *Chem Rev*, 1995, **95**, 735-758.
33. R. S. Kumar, M. Balasubramanian, M. Jacobsen, A. Bommannavar, M. Kanatzidis, S. Yoneda and A. L. Cornelius, *J Electron Mater*, 2010, **39**, 1828-1831.
34. W. Wei, N. Yaru, L. Chunhua and X. Zhongzi, *Rsc Adv*, 2012, **2**, 8286-8288.
35. H. G. S. Yang, Cheng Hua; Qiao, Shi Zhang; Zou, Jin; Liu, Gang; Smith, Sean Campbell; Cheng, Hui Ming; Lu, Gao Qing, *Nature*, 2008, **453**
36. Y. Zhao, C. Li, X. Liu, F. Gu, H. Du and L. Shi, *Applied Catalysis B: Environmental*, 2008, **79**, 208-215.
37. H. Zhang, P. Liu, F. Li, H. Liu, Y. Wang, S. Zhang, M. Guo, H. Cheng and H. Zhao, *Chemistry-A European Journal*, 2011, **17**, 5949-5957.
38. X. Han, Q. Kuang, M. Jin, Z. Xie and L. Zheng, *Journal of the American Chemical Society*, 2009, **131**, 3152-3153.
39. J. Zhu, S. Wang, Z. Bian, S. Xie, C. Cai, J. Wang, H. Yang and H. Li, *CrystEngComm*, 2010, **12**, 2219-2224.
40. J. S. Chen, Y. L. Tan, C. M. Li, Y. L. Cheah, D. Luan, S. Madhavi, F. Y. C. Boey, L. A. Archer and X. W. Lou, *Journal of the American Chemical Society*, 2010, **132**, 6124-6130.
41. H. Zhang, Y. Wang, P. Liu, Y. Han, X. Yao, J. Zou, H. Cheng and H. Zhao, *Acs Appl Mater Inter*, 2011, **3**, 2472-2478.
42. W. Q. Fang, J. Z. Zhou, J. Liu, Z. G. Chen, C. Yang, C. H. Sun, G. R. Qian, J. Zou, S. Z. Qiao and H. G. Yang, *Chemistry-A European Journal*, 2011, **17**, 1423-1427.
43. L. D. Sanchez, S. F. M. Taxt-Lamolle, E. O. Hole, A. Krivokapic, E. Sagstuen and H. J. Haugen, *Applied catalysis. B, Environmental*, 2013, **142**, 662-667.
44. C. Feng, Y. Wang, Z. Jin, J. Zhang, S. Zhang, Z. Wu and Z. Zhang, *New J Chem*, 2008, **32**, 1038-1047.
45. Q. Meng, T. Wang, E. Liu, X. Ma, Q. Ge and J. Gong, *Phys Chem Chem Phys*, 2013, **15**, 9549-9561.